The High-Resolution Wavevector Analysis for the characterization of the dynamic response of composite plates

Pierre Margerit, Arthur Lebée, Jean-François Caron, Kerem Ege, Xavier Boutillon

The High-Resolution Wavevector Analysis for the characterization of the dynamic response of composite plates

Pierre Margerit[a], Arthur Lebée[a,*], Jean-François Caron[a], Kerem Ege[b], Xavier Boutillon[c]

[a]*Laboratoire Navier, UMR 8205, École des Ponts, IFSTTAR, CNRS, UPE, Champs-sur-Marne, France*
[b]*Univ Lyon, INSA-Lyon, LVA EA677, F-69621 Villeurbanne, France*
[c]*Laboratory of Solid Mechanics (LMS), École polytechnique, Palaiseau, France*

Abstract

The High Resolution Wavevector Analysis (HRWA) is presented and its application illustrated. Extending the High Resolution Wavenumber Analysis method [1] to 2D signals, it allows the wide-band and local characterization of the linear elastic behavior of anisotropic plates. The method belongs to the family of experimental wavenumber-based characterization methods and uses the high resolution signal processing algorithm ESPRIT (Estimation of Signal Parameters via Rotational Invariance Techniques) and the ESTER criterion (ESTimation of ERror) to overcome some of the limitation of Fourier-based methods. Three experimental applications on composite plate specimens are presented. First (i), from the out-of-plane velocity field of a sandwich plate with a foam core, different wave types (bending, shear and compression) are extracted. The results are compared with numerical predictions. Second (ii), individual layer contributions are separated on a honeycomb sandwich plate by means of the observation of the dependence of the extracted complex wavevectors as a function of wave propagation direction and frequency. Third (iii), a local wavenumber extraction is performed on a 4-layer carbon-epoxy plate made of fiber patches with spatially varying orientations. The local specific bending stiffness of the plate is identified from the extracted wavevectors and compared with theoretical results.

Keywords: Non-Destructive Evaluation, High-Resolution Methods, Wave Propagation, Composite Structures

1. Introduction

An advanced knowledge of the dynamical behavior of composite materials is needed for a number of applications, ranging from damage identification [2, 3, 4, 5] to material replacement [6, 7] or structural optimization [8, 9, 10]. More specifically, the non-destructive evaluation (NDE) of the linear viscoelastic dynamical behavior of composite structures is an active research field [11].

The whole spectrum of frequencies for which composite structures has to be characterized is usually divided in three regions: (i) the low frequency regime, where the response of the structure can be well described by a reduced number of modes; (ii) the high frequency regime, where the wavelength is so small that the structure can be considered infinite; (iii) the medium frequency regime in which the modal overlap is high and boundary conditions cannot be neglected.

Usually, NDE techniques involves modal analysis in low frequencies [12, 13, 14] while ultrasonic testing is performed in the high frequency regime [15, 16]. In the last decades, the development of full-field

*Corresponding author. *arthur.lebee@enpc.fr*

measurement techniques (i.e. high-speed cameras [17, 18] or scanning Doppler laser vibrometers [19, 20]) allowed for the development of NDE methods that perform well in the medium frequency range. Among these methods, some are based on the knowledge of the properties of the field. One example is the Force Analysis Technique [21, 22, 23] where the partial derivatives of the field are estimated by means of finite difference schemes. Hence they are injected in the governing equations of a structure model to identify its parameters. The variationnal formulation of such approach is the Virtual Fields Method [24, 25], which uses test functions with the principle of virtual works to characterize the structure.

Some other medium frequency methods approximate the measured field with a set of functions. The parameters of these functions usually contains key data for the identification of the structure. For example, Hankel functions are used with the Image Source Method (ISM) to characterize isotropic plates in the steady harmonic regime [26, 27]. As the Green functions of anisotropic plates are not analytic anymore, plane waves are used to approximate the field measured on composite plates. A method based on this principle is the Inhomogeneous Wave Correlation (IWC) method [28, 29].

The latter type of methods is focusing on the identification of guided waves propagating in plates. Indeed, in the medium frequency range (i) the wavelength can be considered large compared to the plate thickness and (ii) the sources as well as the boundary conditions can be considered far enough from the observed location to have a reduced impact on the geometry of the wavefront. Hence the plate can be considered as a waveguide: the wave propagation direction is confined in the plane of the plate and the wavefront is assumed to be contained in a plane orthogonal to the plate. Under these assumptions, it is possible to derive the dispersion equation relating wavevectors to the frequency directly from the constitutive materials and the lay-up of the composite plate (see for instance [30]). It turns out that the parameters of plane waves travelling in a plate (the complex wavevectors and the amplitudes of the corresponding waves) can be extracted from a full-field measurement of the plate steady harmonic response. Such extracted wavevectors reflect the dispersive properties of the plate. By means of an inverse problem, some of its mechanical properties may be identified from experimentally extracted wave parameters. Contrary to modal analysis, the smaller sensitivity of the procedure to boundary conditions and sources makes it a good candidate for in-situ evaluation of structures, when the geometry and the applied loads are not completely known.

The IWC method can be summarized as follows. At a given frequency, a distribution of wave propagation angles is chosen *a priori*. For each given angle, a trial plane wave can be synthesized with a complex wavenumber as parameter. The wavevector is then searched as the complex wavenumer that maximizes the correlation coefficient between the measured plate harmonic response and the synthesized wave. Consequently the identification problem leads to a non-linear optimization scheme, that has to be solved for each wave propagation direction, with the real and imaginary part of the complex wavenumber as optimization parameters. As it is closely related to the Fourier transform, it suffers from the same limitation in terms of wavenumber resolution. This limits the accuracy of the wavevector extraction when only a few wavelengths are contained in the signal. Moreover, as the distribution of the wave propagation angles is fixed *a priori*, the method may return invalid results, when actually no wave propagates in the searched direction.

In the past few decades, some improved signal processing methods suited for the extraction of the complex poles (decaying exponentials) of a measured signal have been developed, such as MUSIC (MUltiple SIgnal Classification) [31], Matrix Pencil [32] and ESPRIT (Estimation of Signal Parameters via Rotational Invariance Techniques) [33]. Built on a signal model, these methods are named *high-resolution*, in the sense that they overcome the intrinsic resolution limitation of the Fourier transform. In particular, the ESPRIT algorithm takes advantage of an invariance property of the signal model to express the wavenumber extraction as the solution of a closed-form problem. In addition, it makes use of the subspace-decomposition technique [34] which allows to predict the *signal order* (number of waves contained in the signal). Subspace-based

methods are widely-used in linear system identification, using for example the state-variable framework [35, 34]. Another example is the ERA [36] (*Eigenvalue Realisation Algorithm*), which is devoted to the identification of the modal parameters of a measured system. A wide range of applications of the ESPRIT algorithm can be found in array processing and radar applications [37, 38], audio processing [39, 40], characterization of structures through modal analysis [12, 13, 23], musical acoustics applications [41, 42, 43, 44] and high-resolution spectral analysis [45]. To be fully efficient, the ESPRIT algorithm must be combined with a criterion dedicated to the the estimation of the signal order, such as the ESTER criterion [46] (ESTimation of ERror)

In a recent article [1], the authors proposed the High Resolution Wavenumber Analysis method (HRWA). Using the ESPRIT algorithm with the ESTER criterion, it allows to extract wavenumbers in the harmonic response of a beam. From these wavenumbers, some equivalent mechanical properties of the beam can be identified. The enhanced performances of this experimental wavenumber-based characterization method are demonstrated: the frequency range of validity is wider, a number of beam motions can be separated (bending and twist), and the wavenumber extraction is faster than in existing methods. However, its application is limited to wavenumber extraction in 1D structures.

In the present work, the method is extended to 2D signals and thus is renamed High-Resolution *Wavevector* Analysis. At a given frequency, it assumes that the harmonic response of a plate is a finite sum of decaying plane waves. Using the 2D version of the ESPRIT algorithm [38], the complex wavevectors are extracted from the measured harmonic response of a plate (e.g. velocity or displacement field), or a portion of its domain. The signal order is estimated thanks to the 2D version of the ESTER criterion [47]. In comparison to Fourier based wavevector estimation methods, the high-resolution properties of the ESPRIT algorithm allow the extraction of wavevectors in low frequencies, where the wavelengths are usually large. In addition, the size of the observation window (partial zone of the measured plate field used as input) can be reduced to extract local wavevectors that can be used to characterize a local plate behavior. The automated estimation of the signal order allows the identification and the separation of multiple wave types: bending, shear or longitudinal waves. No assumption has to be made on the distribution of the wave propagation angles, as these angles are part of the estimated parameters. Finally, by formulating the wavevector extraction problem as a closed-form problem, no optimization scheme is involved and thus the wavevector extraction is computationally efficient and robust.

When the method is applied on beams [1] the signal model corresponds exactly to the harmonic response of the structure, as long as it can be considered as a waveguide in the frequency range of interest. In two dimensions, the wavefront is not necessarily a straight line. Therefore, the local 2D signal may not be represented exactly by a finite sum of decaying plane waves. The influence of this approximation on the extracted wavevectors is not clear at this time. It was experimentally observed that the impact of a non-straight wavefront is mostly contained in the imaginary part of the extracted wavevectors. As a consequence, a criterion based on the spatial decay of the extracted waves is proposed to discard the wavevectors with a dominant imaginary part and thus diminish the influence of the signal model approximation error on the identification results.

The paper is organized as follows : in Section 2 the HRWA is presented. In Section 3, several experimental applications of the method to different composite plates are presented to illustrate its possibilities. First, from an orthotropic sandwich plate, several kinds of waves are extracted (bending, in plane shear and compression), and the results are compared to numerical predictions. Second, on a honeycomb sandwich plate, the bending waves are studied and a particular frequency-dependent anisotropic behavior is observed, related to the mechanical properties of individual layers. Third, a local wavevector extraction is performed on a spatially inhomogeneous composite plate made of 36 patches with various fiber orientations. Using the

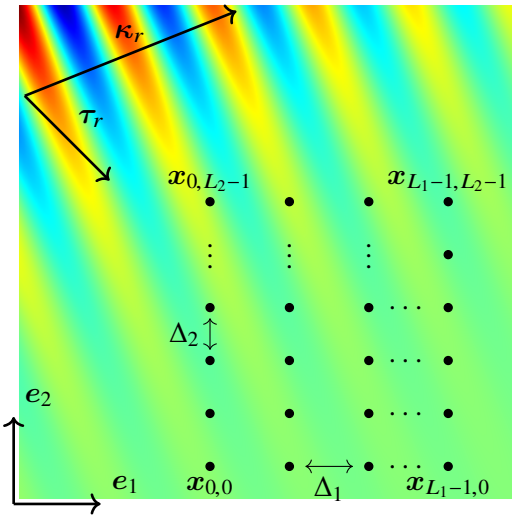

Figure 1: Schematic representation of a measurement mesh grid $\boldsymbol{x}_{nm}$ suited for the HRWA. A decaying plane wave is represented, with its complex wavevector $\boldsymbol{k}_r = \boldsymbol{\kappa}_r + \mathrm{i}\,\boldsymbol{\tau}_r$.

Classical Lamination Theory, an inverse problem is formulated, leading to the identification of the equivalent specific bending stiffness of the plate at many different patch locations. The potential of the method to identify local structural behaviors, given by fiber direction, stacking sequence and material properties is illustrated.

2. High Resolution Wavevector Analysis

Both ESPRIT algorithm and ESTER criterion are well-established in the signal processing community [38, 48]. As a consequence, minimal details are given in this section. However, both algorithms are developed in AppendixA in order to give all the content needed for the implementation of the HRWA.

Along this paper, the HRWA is applied to the harmonic response of a plate. Basically, a collection of harmonic response fields can be obtained by computing the Fourier transform of the measurement of the time-dependent response field of a plate. The wavevector extraction procedure is then performed for each given frequency ω. For the sake of readability, the dependence on ω is omitted in the following, unless required for clarity.

2.1. Signal model

The harmonic response field $s(\boldsymbol{x})$ of a plate, or a sub-domain of a plate, is modeled as a sum $u(\boldsymbol{x})$ of R plane waves and some uncorrelated noise $b(\boldsymbol{x})$. The signal model is expressed as follows:

$$s(\boldsymbol{x}) = u(\boldsymbol{x}) + b(\boldsymbol{x}) = \sum_{r=1}^{R} a_r \, \mathrm{e}^{\mathrm{i}\,\boldsymbol{k}_r \cdot \boldsymbol{x}} + b(\boldsymbol{x}) \tag{1}$$

where R is the *signal order* and the a_r are the complex amplitudes related to the waves. The related complex wavevector $\boldsymbol{k}_r$ is written as:

$$\boldsymbol{k}_r = k_{1,r}\,\boldsymbol{e}_1 + k_{2,r}\,\boldsymbol{e}_2 = \boldsymbol{\kappa}_r - \mathrm{i}\,\boldsymbol{\tau}_r \tag{2}$$

where the two complex numbers $k_{1,r}$ and $k_{2,r}$ are the wavenumbers in each dimension of the signal (see Fig. 1).

The phase velocity vector $\boldsymbol{c}_r$ can be retrieved from the wavevector and the frequency:

$$\boldsymbol{c}_r = \frac{\omega}{|\boldsymbol{k}_r|^2}\boldsymbol{k}_r^* \tag{3}$$

as well as the wavelength vector:

$$\boldsymbol{\lambda}_r = \frac{2\pi}{|\boldsymbol{\kappa}_r|^2}\boldsymbol{\kappa}_r \tag{4}$$

where $\bullet^*$ denotes the complex conjugate.

The decay of the plane waves along their propagation is related to the imaginary part $\boldsymbol{\tau}_r$ of the wavevector. Since the decay is not necessarily maximum in the wave propagation direction [49], the real and imaginary parts $\boldsymbol{\kappa}_r$ and $\boldsymbol{\tau}_r$ of the complex wavevector are not necessarily colinear. However, it is of common use to define the spatial decay ratio γ:

$$\gamma_r = \frac{|\boldsymbol{\tau}_r|}{|\boldsymbol{\kappa}_r|} \tag{5}$$

The extracted spatial decay may have several causes. Indeed, three main contributions can be expected: the first contribution is the energy loss along the propagation of the wave, due to viscous materials or fluid-structure interaction. Second, some evanescent waves are present close to boundaries, accounting for the boundary conditions. Third, $\boldsymbol{\tau}_r$ is influenced by the geometry of the sources. For example, a point source located at $\boldsymbol{x}_p$ in an isotropic conservative plate generates a circular wavefront with a spatially-dependent amplitude $a_r(\boldsymbol{x}) \propto |\boldsymbol{x} - \boldsymbol{x}_p|^{-1/2}$, which has an influence on the identified wave decay. Evaluating how these effects contribute to $\boldsymbol{\tau}_r$ is beyond the scope of this article. Therefore, the imaginary part of the extracted wavevectors is not considered in the applications of the HRWA presented in this paper, except when the signal corresponds closely to a plane wave (see 3.2).

Let us recall that the signal model is formulated so that a different set of the parameters $\{\boldsymbol{a}_r, \boldsymbol{k}_r, R\}$ will be identified at each frequency. Consequently, virtually any dependence of these parameters can be identified as a function of frequency, regardless of the wave dispersion in the structure.

2.2. Regular grid mesh of measurements

In order to be able to apply the 2D ESPRIT algorithm [38] (Estimation of Signal Parameters via Rotational Invariances Techniques), the signal $s(\boldsymbol{x})$ has to be measured along a 2D regular mesh grid $\boldsymbol{x}_{nm}$ of step $\{\Delta_1, \Delta_2\}$ (see Fig. 1):

$$\boldsymbol{x}_{nm} = \boldsymbol{x}_{00} + n\,\Delta_1\boldsymbol{e}_1 + m\,\Delta_2\boldsymbol{e}_2 \tag{6}$$

with $(n, m) \in [\![\, 0, L_1 - 1 \,]\!] \times [\![\, 0, L_2 - 1 \,]\!]$. The signal matrix $\boldsymbol{S}$ is formed with the acquired data:

$$S_{nm} = s(\boldsymbol{x}_{nm}) \tag{7}$$

and is processed by the ESPRIT algorithm (see AppendixA.1).

Aliasing can lead to an ambiguity about the magnitude of the extracted wavevector. As a consequence, the Nyquist criterion has to be fulfilled to avoid ambiguities: each individual wave contained in the signal must have a wavelength larger than twice the grid spacing:

$$\begin{aligned} \boldsymbol{\kappa}_r \cdot \boldsymbol{e}_1 &< \frac{\pi}{\Delta_1} \\ \boldsymbol{\kappa}_r \cdot \boldsymbol{e}_2 &< \frac{\pi}{\Delta_2} \end{aligned} \tag{8}$$

2.3. *Wavevector extraction*

In the ESPRIT algorithm (summarized in AppendixA.1), the invariance properties of the signal are used to estimate the wavevectors thanks to matrix operations. As a consequence, the wavevector extraction is formulated as the solution of a closed-form problem. Knowing the signal order R, the application of the ESPRIT algorithm results in the identification of the parameters of R decaying plane waves. However, the signal order is unknown in practice, which could compromise the estimation of the wavevectors.

For the estimation of the signal order R without *a priori* knowledge, Badeau [46] devised of the ESTER criterion (*ESTimation of ERror*), for a 1D signal. The ESTER criterion is based on the error made on the estimation of the invariance property of the signal by the ESPRIT algorithm, for a given signal order r. By estimating this error for $r \in [\![1, r_{\max}]\!]$, the signal order R is chosen so that it minimizes the estimation error of the invariance property. Multidimensional extensions of this criterion have been proposed [47], computing the arithmetic or geometric mean of the errors in the different signal dimensions. Further details concerning the computation of the criterion are given in AppendixA.2.

The wavevector extraction procedure, implemented in order to achieve the High Resolution Wavevector Analysis, is summarized in AppendixA.3. An example of application is illustrated in Figure 2. The procedure is applied to the harmonic response of the orthotropic composite plate sample, studied in 3.1, at the frequency of 250 Hz (Figure 2.(a)). The ESTER criterion (inverse of the geometrical mean of the estimation errors) is computed for $r \in [\![1, 30]\!]$ (Figure 2). A maximum of the criterion can be observed for $R = 4$. Finally, four wavevectors are extracted with the ESPRIT algorithm (dot marks in Figure 2.(b)).

Thanks to the ESTER criterion, which uses the same theoretical framework as the ESPRIT algorithm, an automated estimation of the signal order R is obtained, if the truncation error is sufficiently contrasted. In this signal order determination procedure, the higher hypothetical signal order $r_{\max}$ has to be chosen. In practice, this parameter must remain low: a high $r_{\max}$ would involve a high computational burden while increasing the risk of extracting spurious wavevectors originating from noise. Moreover, it is of common knowledge that the ESPRIT algorithm performs well for a reduced number of poles [50]. This parsimony requirement seems contradictory with the infinite number of plane waves that would be needed to represent

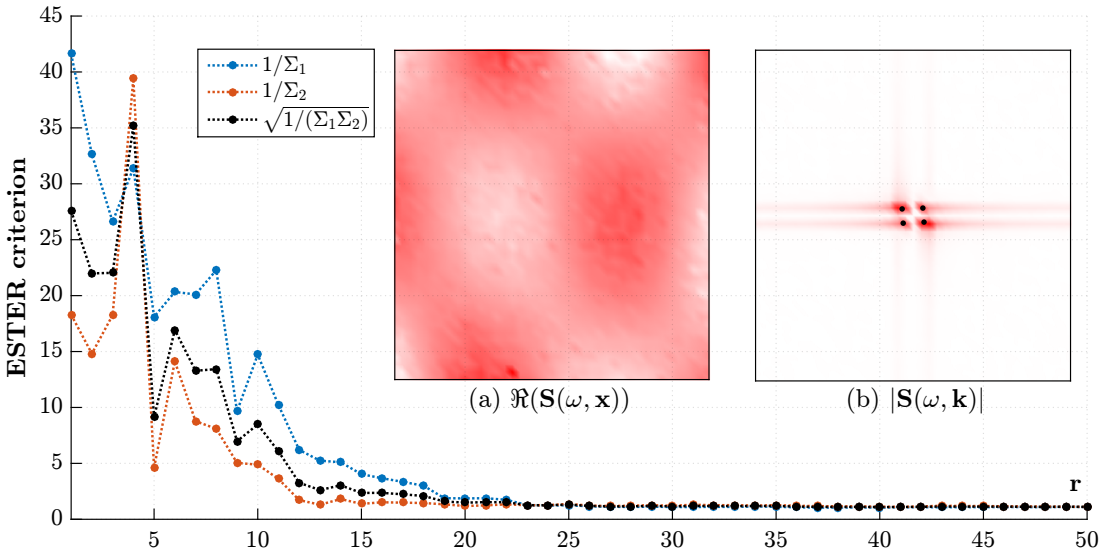

Figure 2: Signal order estimation. The signal $\boldsymbol{S}(\omega, \boldsymbol{x})$ (a) is measured on the orthotropic sandwich plate of Section 3.1, at the frequency of 250 Hz. The ESTER criterion is computed (eqs. A.15 and A.16) for $r \in [\![1, 30]\!]$, and the signal order R chosen at the local maximum $r = 4$. Finally, four wavevectors are extracted with the HRWA (markers in (b))

a given complex physical situation. In practice, the reflection of waves at the boundaries of the plate creates destructive and constructive interferences responsible for a selection process in the wavevectors. As a consequence, it was observed that the plate response can be well approximated by a reduced number of wave components (typically less than a few dozen) if the effect of losses remains low. Special care must be taken when the damping is high or when the source is close to the observation window in order to keep the signal order reasonably low (see example 3.2). Therefore, R represents the *apparent* number of plane-waves in the observed vibration-field. All along the examples shown in this paper, the parameter $r_{\max}$ was chosen equal to 30.

2.4. Signal preprocessing

Before the application of the wavevector extraction procedure described before, it is possible to perform additional preprocessing steps on the measured signal. Indeed, because of the the signal parsimony needed to apply the ESPRIT algorithm, only the dominant components in terms of energy (corresponding to the highest eigenvalues of the covariance matrix) are identified when noise is added to the signal. As a consequence, waves with a low amplitude can be hard to extract from the signal. To that end, sub-band decomposition techniques have been proposed [51] as pre-processing steps.

These sub-band decomposition techniques consist in performing some spatial filtering on the measured signal. In the case of interest here, a 2D Finite Impulse Response filter $\boldsymbol{F}$ (FIR) can be convoluted to the signal $\boldsymbol{S}$ as follows:

$$\tilde{\boldsymbol{S}} = \boldsymbol{S} * \boldsymbol{F} \tag{9}$$

This technique can help to overcome the limitation mentionned above. If the wavevectors corresponding to high and low amplitude waves are well separated, they can be isolated. Depending on the chosen filter shape (i.e. band-pass filter with $k_{\min}$ and $k_{\max}$ as parameters), waves with a high amplitude can be filtered so that applying the ESPRIT algorithm on the signal $\tilde{\boldsymbol{S}}$ allows to extract low amplitudes waves. Moreover, filtering can also help to reduce the number of component in the signal, thus improving the ESPRIT algorithm performance. However, this filtering step should be used carefully as it can introduce some artifacts due to the non-zero signal values at boundaries. Even if a windowing step can be performed before filtering, these artifacts could lead to the extraction of spurious wavevectors.

As an example, this filtering technique is performed in the following to separate waves corresponding to in-plane and out-of-plane motion (see Section 3.1).

2.5. Wavevector selection

Most of the energy related to *nearly* evanescent waves (such that $|\boldsymbol{\tau}_r| > |\boldsymbol{\kappa}_r|$) is contained close to sources and boundaries, which represents a small part of the overall processed signal. Also, $\boldsymbol{\tau}_r$ is sensitive to noise. In addition, as discussed above, $\boldsymbol{\tau}_r$ has several contributions that may be difficult to separate and may be related to signal model errors. Moreover, the uncertainty associated to the wavevectors extracted with the ESPRIT algorithm increases rapidly for $\gamma_r > 10\%$ [52]. As a consequence, a selection step must be performed to keep only the wavevectors with a dominant real part. We choose to keep only the waves with an equivalent decay factor γ_r Eq. (5) satisfying:

$$\gamma_r \leq \gamma_{\max} \tag{10}$$

This strategy can be used when the observed zone of the plate is small, or close to any source or boundary, where spurious evanescent waves may be present. Considering plates made of materials with low loss factors, a reasonable choice for $\gamma_{\max}$ is 10%, corresponding to situations where the effect of losses

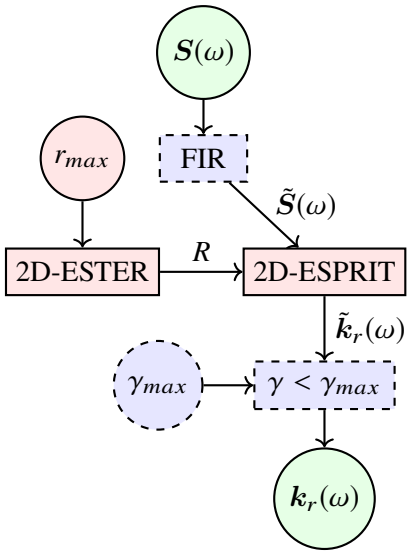

Figure 3: Block diagram of the HRWA. Optional processing steps are in blue.

are small and do not alter the real part. In the present work, it is applied in the local wavevector extraction performed in Section 3.3.

A block diagram representing the High-Resolution Wavevector Analysis steps is shown in Figure 3. The procedure can be summarized as follows: The harmonic response field $s(\omega, \boldsymbol{x})$ of a plate, or a subpart of a plate, is measured on a regular grid of points $\boldsymbol{x}_{nm}$ (Eq. (6)), giving the signal matrix $\boldsymbol{S}(\omega)$ (Eq. (7)). Before the application of ESPRIT algorithm, some spatial filtering can be achieved (Eq. (9)) to separate different kinds of waves which wavevectors are distinct. Next, the wavevector extraction procedure (see AppendixA.3), performed at a given given frequency ω, leads to the extraction of a discrete spectrum of R complex wavevectors $\boldsymbol{k}_r$ (Eq. (2)), where R depends on the frequency. Finally, in order to characterize the properties of the plate with a good accuracy, the evanescent wavevectors can be discarded (Eq. (10)).

Finally, from the collection of obtained wavevectors at all frequencies, discrete experimental dispersion surfaces are obtained in the $(\boldsymbol{k}, \omega)$ space, characteristic of the local plate behavior.

In comparison with Fourier-based wavevector extraction analysis, the HRWA presents some improvements:

1. *High-resolution:* the HRWA overcomes the resolution limitations of Fourier-based methods. This improvement allows the extraction of plane waves which wavelength is comparable or even larger than the observing window size. As a consequence:
   (a) the low-frequency limit of wavevector-based observations is reduced, allowing for the characterization of plates in a wide frequency range, from the first modal frequencies and without *a priori* limitation on high frequencies (as long as it can be considered as a waveguide).
   (b) the observation window can be reduced to characterize local plate behavior by means of locally extracted wavevectors. Plates with slowly spatially varying mechanical properties can be characterized.
2. *Automated signal order choice:* thanks to the ESTER criterion, the number R of waves necessary to approximate the signal is estimated, in the range $[\![1, r_{\max}]\!]$. As a consequence:
   (a) the wave propagation direction distribution is directly identified: $2R$ poles are extracted simultaneously and paired to form wavevectors, with given propagation directions.

Material	Thickness	E_L	E_T	G_{LT}	ν_{LT}	ρ
HD PVC Foam	5.2 mm	80 MPa	80 MPa	32 MPa	0.25	86 kg/m^3
Prepreg Carbon	150 μm	120 GPa	6.5 GPa	3.5 GPa	0.35	1300 kg/m^3

Table 1: Indicative mechanical properties of the materials of plates.

(b) multiple wave types (e.g. bending, in-plane motions) can be separated. This allows for the characterization of multiple plate strain mechanisms.

3. *Linear problem:* The wavevector extraction is formulated as a closed-form problem. As a consequence:
   (a) the robustness of wavevector extraction is ensured.
   (b) no assumption is needed neither on the wavevector nature (real, complex, real and imaginary part colinearity) nor on their dependence as a function of frequency.

3. Applications

Throughout three application cases, the following Section illustrates the interest of the HRWA as a characterization tool of the linear dynamic behavior of composite plates. The plates were fabricated at the Laboratoire Navier: two homogeneous sandwich plates with Carbon Fiber Reinforced Polymer (CFRP) skins and different core materials (HD PVC foam for plate 1 and Honewcomb for plate 2), and one inhomogeneous 4-layers laminated CFRP plate consisting of 36 spatially distributed patches with varying fiber directions. Carbon prepreg was used. The in-plane mechanical engineering constants of the materials, identified with static tensile tests, are summarized in Table 1.

For all plate specimens, the out-of-plane velocity field was measured along regular grids with a Scanning Laser Doppler Vibrometer (SLDV model Polytec PSV-400). The instantaneous velocity of the surface of the plate is measured by repeating the experience for each point of the grid. A stationary signal (band pass filtered noise) was used as excitation signal, in order to stimulate a wide range of frequencies. To improve the signal to noise ratio, the transfer function between the measured velocity and the electrical signal is taken. Furthermore, multiple realizations of the measurement are performed at each point. The average over the realizations is taken as data to build the signal matrix processed in the ESPRIT algorithm (see AppendixA.1).

3.1. Sandwich Plate with foam core

3.1.1. Plate Configuration

The first experimental study focuses on the characterization of a square sandwich plate 60 cm wide, with a High Density PVC foam core and two thin carbon skins of one layer each. The fibers are oriented in the 90° direction. A scheme of the plate is shown in Figure 4. Indicative material properties of the HD PVC foam and carbon prepreg are summarized in Table 1. Only in-plane engineering constants are shown: out-of plane constants can be deduced for the HD PVC core, which is isotropic. The transversely isotropic carbon prepreg is used for the skins (assuming $\nu_{TT} = 0.3$), in which in-plane strains and stresses are dominant. This particular sandwich plate architecture is chosen because of its high anisotropy and the high contrast between the stiffness of its core and skins. In addition, it is homogeneous in the plate directions, which allows the comparison of experimental results with numerical predictions of the propagation of plane waves in multilayered plates.

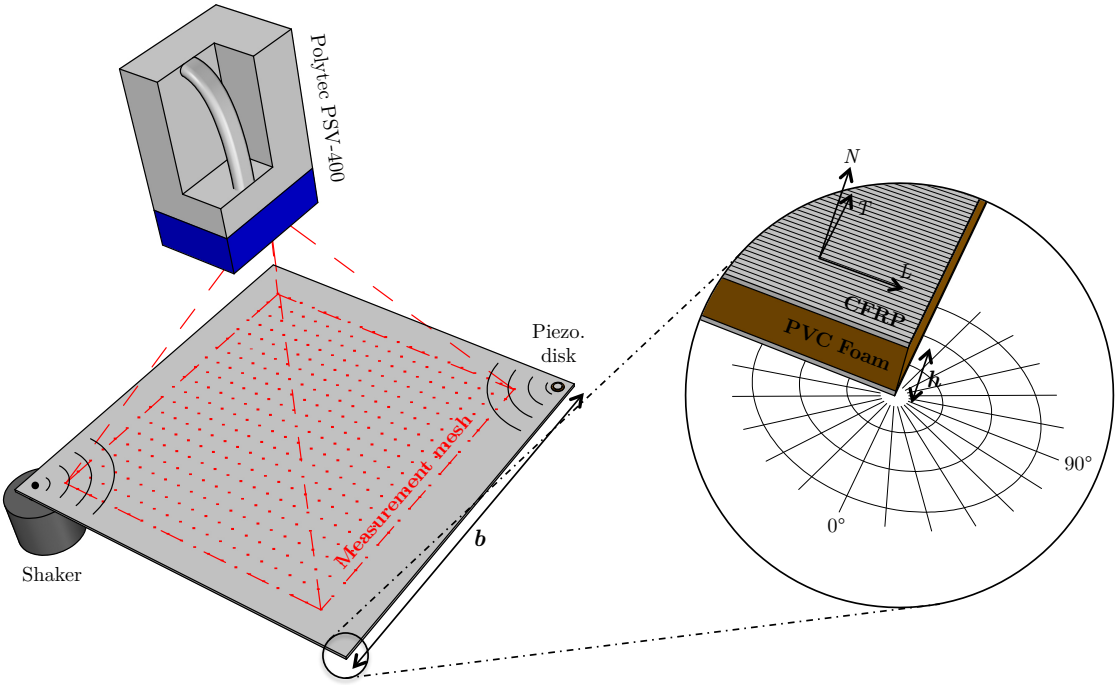

Figure 4: Orthotropic sandwich plate with HD PVC foam core. Scheme of the measurement setup with a closeup on the plate configuration. The two CFRP skins are oriented at 90°. $h = 5.5$ mm, $b = 60$ cm.

3.1.2. Measurement setup

A scheme of the measurement setup is given on figure 4. The plate is excited simultaneously by a shaker and a piezoelectric disk attached at opposite corners in order to excite a wide range of frequencies: from 100 Hz to 40 kHz. The measuring grid is 175×175 points ($\Delta = 3.4$ mm), fulfilling the Nyquist criterion (Eq. (8)) at the higher observed wavenumber ($k_{\max} \approx 600$ rad.m^{-1}, $\lambda_{\min} \approx 10$ mm from Eq. (4)). Repeating the measurement 10 times at each point, the total measuring time duration is approximately two hours. After the computation of the time Fourier transform of the signal, 1600 plate harmonic responses are available, for frequencies between 100 Hz and 40 kHz.

3.1.3. SFEM scheme

In this section, the experimental HRWA results are compared with the results of a Spectral Finite Element Method (SFEM) scheme. Introduced by Shorter [30] for isotropic laminated plates, the SFEM has been extended to laminated plates made of orthotropic layers with arbitrary orientation [53]. A more general scheme, for waveguides of arbitrary cross-section, can be found in [54], also referred to as the Semi Analytical Finite Elements (SAFE) method. At a given frequency ω, and for a given wave propagation angle ϕ, the plate displacement field $\boldsymbol{u}$ is assumed of the form:

$$\boldsymbol{u}(\boldsymbol{x}, t) = \boldsymbol{U}(x_3)\, \mathrm{e}^{\mathrm{i}(\omega t - k(\cos(\phi)x_1 + \sin(\phi)x_2))} \tag{11}$$

The SFEM uses finite elements to compute the guided modes $\boldsymbol{U}(x_3)$, as the result of a quadratic eigenvalue problem in the wavenumber k. The SFEM predictions shown in this section are computed with the material properties in Table 1 as input. These properties are assumed independent from the frequency. The SFEM convergence was verified in the frequency range of interest, with a mesh composed of 3 elements in each skin and 100 elements in the core (element length ≈ 50 μm). The results shown in the following are obtained by performing SFEM computations for a given set of wave propagation angles ϕ and frequencies ω.

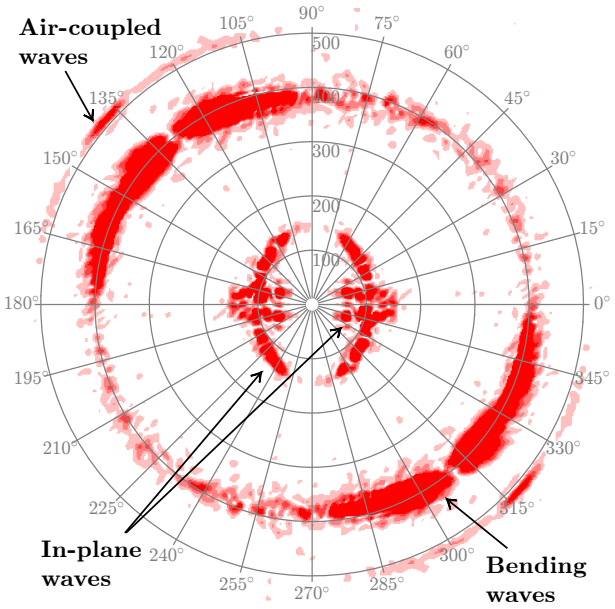

Figure 5: Orthotropic sandwich plate with HD PVC foam core. Wavevector Fourier spectrum corresponding to the measured harmonic velocity field at the frequency of 28 kHz. Four wave types can be seen: in-plane (compression and shear), bending and air-coupled waves.

3.1.4. Results

The wavevector Fourier spectrum (result of a 2D spatial Fourier transform applied to the measured harmonic field) corresponding to the frequency of 28 kHz, is shown in Figure 5. Four high intensity regions can be distinguished and related to different wave types. From low to high wavenumber: two types of in-plane motion, bending motion, and air-coupled waves. It can be observed that the higher spatial spectrum amplitudes corresponding to bending and air-coupled waves are found in the upper-left and bottom-right regions. This is due to the position of the two sources, at the upper-left and bottom-right corners of the plate. As a consequence of the wave decay and since the wavelength decreases with the frequency, reflected waves weaken so that the direct contribution of the sources dominates the response of the plate. This can be noticed on the HRWA results too (see Figures 6 and 8). By contrast, the in-plane waves show a relatively large wavelength so that the wave intensity is more equally distributed and the source less visible. More details are given in the discussion below.

This first study focuses on the conservative behavior of the sandwich plate. Since the damping is low in this plate, only the real part $\boldsymbol{\kappa}$ of each wavevector is taken into account in Eq. (3) to compute the vectorial phase velocity $\boldsymbol{c}$ of each extracted wave. All the experimental results discussed below are extracted from the same collection of measured plate harmonic responses.

Bending motion. The dominant source of out-of-plane velocity comes from the bending motion. As a consequence, in the studied frequency range, applying the HRWA to the measured signal without spatial filtering (Eq. (9)) leads to the extraction of bending wavevectors. The phase velocity $\boldsymbol{c}$ of these waves is plotted in Figure 6. In Figure 6a, $\boldsymbol{c}$ is represented in a polar diagram for 10 frequencies covering the frequency range. Hence the dependence of the wave velocity as a function of its propagation direction can be studied. Numerical predictions (solid lines) are added to the HRWA results (dot marks). In Figure 6b, the magnitude of the phase velocity of all extracted waves is plotted as red markers. Numerical lowest and highest phase velocities (SFEM results at 0° and 90°) are added as black lines.

To interpret the results, the slenderness ratio is defined as the ratio of the wavelength λ over the plate thickness h. It is is large at low frequencies ($\lambda/h \approx 160$ at 500 Hz) thus the plate behaves as a thin plate. In this regime, the bending wave velocity is proportional to the square root of the frequency. Moreover, the bending motion is source of in-plane stresses which are mostly contained in the carbon fiber skins. As a consequence, the anisotropy of the phase velocity diagram is high and is symmetric with respect to the fiber direction (90°). As the frequency increases, the wavelength decreases and the slenderness ratio as well ($\lambda/h \approx 8$ at 10 kHz, ≈ 4.5 at 20 kHz, ≈ 2.3 at 40 kHz). The plate consequently behaves as a thick plate: out-of-plane shear strains, mostly contained in the foam core, become more and more significant [55]. As the foam can be considered isotropic in the frequency range of interest, the bending wavevector magnitude tends to be independent of the wave propagation angle. In addition, as the shear effects are not dispersive, the bending velocity tends asymptotically toward a constant value.

In-plane motions. Laminated plates can exhibit coupled behavior between in-plane and out-of-plane motions, when the symmetry to the neutral plane is not exactly satisfied. Imperfect fabrication or piezoelectric disk used as source can break the plate mirror symmetry. In addition, longitudinal waves can be the source of out-of-plane displacement, because of the out-of-plane Poisson effect. Finally, the SLDV velocity measurement may contain contributions from the in-plane components of the plate motion, when the laser beam is not exactly normal to the plate surface. When performing modal analysis, these contributions can be an issue, as they are not separable from the out-of-plane kinematic field, without a proper 3D velocity measurement. With the proposed HRWA, bending and in-plane motions can be isolated because of their well separated wavevector magnitudes.

To perform the extraction of in-plane motion waves with the HRWA, the contribution of the bending waves in the signal has to be removed because of their relatively high amplitude. To this end, a 2D spatial

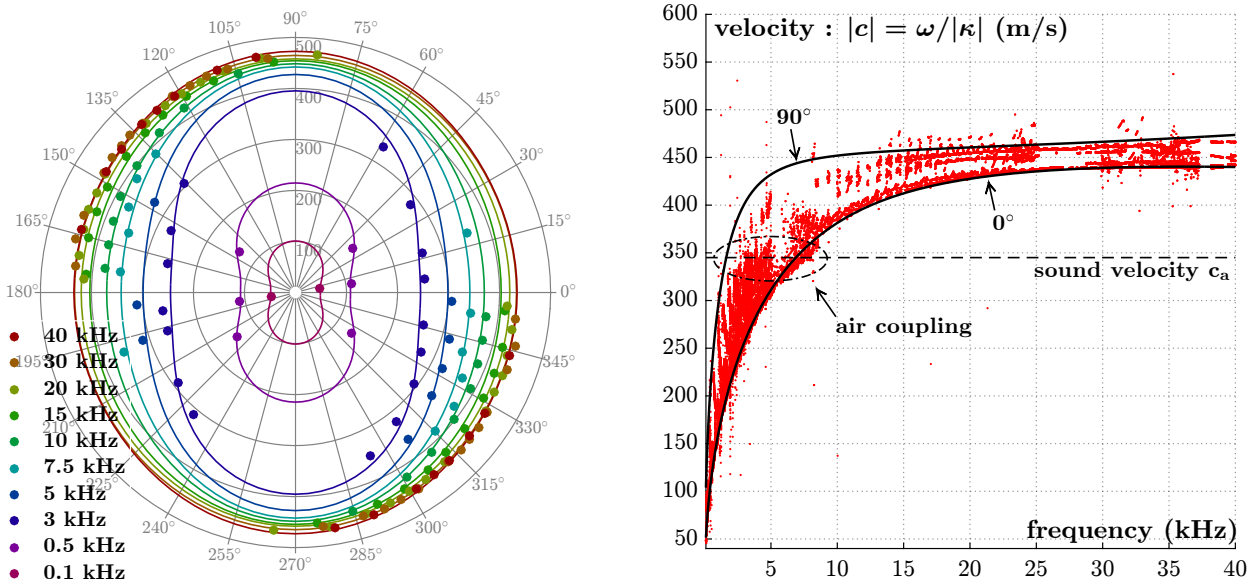

(a) (b)

Figure 6: Orthotropic sandwich plate with HD PVC foam core. Vectorial phase velocities $\boldsymbol{c}$ of bending waves (m/s). Dot marks: HRWA results applied on measurements. Solid lines: numerical wavevector results computed with a SFEM scheme ([53]). (a) Phase velocities at 10 different frequencies between 100 Hz and 40 kHz, as function of the propagation direction. (b) Magnitude of all extracted phase velocities as function of the frequency. Highest and lowest velocities computed with SFEM (resp. at 90° and 0°) are plotted as solid black lines.

low-pass filter is applied on the signal (Eq. (9)). As the bending wavevectors were extracted previously, they are used to tune the cutoff wavenumber of the filter: at each frequency, the cutoff wavenumber is chosen as a fraction of the minimum bending wavevector extracted at this frequency. Using this strategy, in-plane motion wavevectors are extracted for frequencies between 28 kHz and 40 kHz.

In Figure 7, the experimentally extracted phase velocities Eq. (3) are plotted as colored dot marks, the color denoting frequency. The experimental results are compared to velocities computed with the SFEM scheme (at 34 kHz). Two kinds of waves can be separated: longitudinal waves (P waves) and in-plane shear SH waves. It can be noticed that a very few wavevectors corresponding to longitudinal waves were extracted for $\phi = [60°, 120°]$. Indeed, the in-plane tensile stiffness of the plate is very high at these angles because of the carbon fibers oriented at 90°. Consequently, longitudinal waves travelling in these directions have a low amplitude and a large wavelength which make them difficult to extract.

As a first approximation, the in-plane motion waves can be considered as non dispersive in the frequency range of interest: their phase velocity depends only on the wave propagation direction. Again, the polar diagram displays two symmetry planes at 0° and 90°, corresponding to the plate orthotropy. Looking closer, some dispersion can be observed in the diagram of the P waves. At the lowest frequencies (blue shade markers), the phase velocity magnitude is larger than at the highest frequencies (red shade markers). This dependence is related to the out-of-plane Poisson effect, which tends to increase with the frequency.

Air-Coupled Waves. The out-of-plane motion of the plate is transmitted to the surrounding air, resulting in an acoustical field which in turn loads the plate. The out-of-plane motion of the plate is transmitted to the surrounding air, resulting in an acoustical field lightly loading the plate (weak coupling). It is well known that the plate-air coupling is very weak when the speed of the bending waves is below the speed of sound in air (subsonic waves, very close to in-vacuo waves) and becomes more efficient (but still in the light-fluid approximation) when the speed of the bending waves becomes larger than the sound speed. The low mass

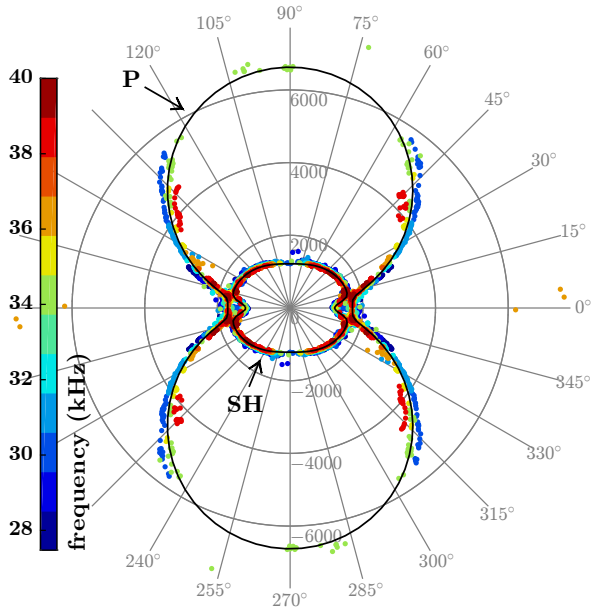

Figure 7: Orthotropic sandwich plate with HD PVC foam core. Phase velocitiy of in-plane motion waves as a function of the wave propagation direction and for frequencies between 28 kHz and 40 kHz: in-plane shear SH waves (inner contour) and longitudinal P waves (outer contour). Dot marks: HRWA results applied to measurements, with colors corresponding to frequency. Solid lines: numerical wavevector results computed with the SFEM scheme at 34 kHz ([53]).

per unit surface of the sandwich plate (840 g/m^2) increases the coupling also. In Figure 6b, the approximate sound velocity is denoted by a horizontal dashed line. Between 5 kHz and 10 kHz, identified bending wave phase velocities (red dots) seems to differ from SFEM numerical results, some of the experimental results being lower than the lowest predicted phase velocity. At these frequencies, the sound velocity coincides with the velocity of some of the bending waves. As a consequence, some extracted wavevectors may be related to waves travelling in the surrounding air. At higher frequencies (>10 kHz), bending wave velocity is higher than sound velocity. Hence their different wavevectors can be separated (see, for example, the result at 28 kHz in figure 5). By applying an appropriate 2D high-pass spatial filter to the velocity field (Eq. (9)), the wavevectors $\boldsymbol{k}_{\mathrm{a}}$ related to air-coupled waves can be isolated. The mean velocity of these particular waves is identified to be approximately c_a = 345 m/s (see Fig. 8), which may slightly differ from the sound velocity because of the fluid loading (see for example [56], p. 237).

This study shows how different kinds of waves can be separated and identified with the HRWA. Thanks to its high-resolution aspects, the bending wavevectors are extracted in a wide frequency range (100 Hz to 40 kHz), even when only a few wavelengths are contained in the measured signal. In-plane motion waves can be extracted and analyzed. Finally, the sound speed is retrieved, as a consequence of the plate coupling with the surrounding air.

All these experimental results are compared with SFEM predictions computed from the mechanical properties of the plate constitutive materials and match closely. In this example, no inverse identification of the mechanical properties was done. However, the good fit between the HRWA and numerical results gives an insight into the potential of wavevector extraction for anisotropic plate characterization. The wavevectors could be used to identify the plate constituent properties via an inverse problem, without much attention paid to excitation sources or boundary conditions. In particular, the ability to separate various plate wave types may allow to identify each layer properties, as the contribution of individual layers to the overall stiffness and inertia is different for each wave type.

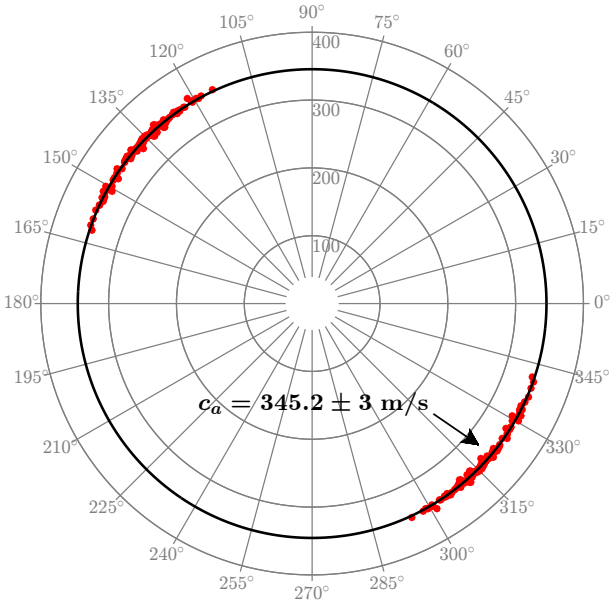

Figure 8: Orthotropic sandwich plate with HD PVC foam core. Sound velocity c_{a} (m/s) measured from extracted wavevector for different frequencies. HRWA results: dot marks ; mean value : solid line

3.2. *Sandwich plate with honeycomb core*

A second experimental study is performed on a square sandwich plate 60 cm wide, with carbon fiber skins oriented at 0° and a honeycomb core (see Figure 9a). The light honeycomb core, with a cell diameter of approximately 7 mm, separates the two stiff skins, leading to a plate with high bending stiffness to weight ratio. This architecture is chosen in order to illustrate the ability of the HRWA to capture individual layer properties: the distinct anisotropic properties of the carbon fiber skins and the honeycomb core result in a particular dependence of the wavevectors as a function of frequency and wave propagation direction.

The velocity field measurement is achieved with a SLDV on a grid of 157×157 points. The Nyquist criterion, verified *a posteriori*, is satisfied. As excitation source, a piezoelectric disk is glued near the center of the plate, which is suspended with two thin rubber bands. Figure 9b gives the measured velocity field at 25 kHz. Because of the significant damping of the plate, few reflections occur and the field is dominated by the direct emission of the source.

Placing the excitation close to the plate center allows the extraction of wavevectors in the surrounding of the source. As a consequence, the wavenumber extraction procedure is applied on 100 reduced zones of the measured field distributed around the source. In Figure 9b, 20 of these zones are represented. The wavevector extraction is performed for each individual zone. As the zones are chosen at a certain distance of the source, the field in each zone corresponds closely to a plane wave. Choosing zones closer to the excitation would yield an imaginary part of the extracted wavevectors more influenced by the rather circular source wavefront. Sufficiently far from the source, the HRWA allows to identify the decay γ (Eq. (5)) of a plane wave along its propagation direction.

A large collection of wavevectors is obtained, which are represented as a function of the wave propagation direction and the frequency in Figure 10a. Both the real and imaginary parts of the extracted wavevectors are represented as dot marks in 3D. This representation of the results makes the dispersion surfaces of the structure clearly visible. In order to help the interpretation of the results, an alternative plot is shown in figure 10b: the magnitude of the real part of the wavevectors $\|\boldsymbol{\kappa}\|$ and the spatial decay γ are represented as a function of the frequency (y-axis) and the wave propagation direction ϕ (color of the dot marks). As the

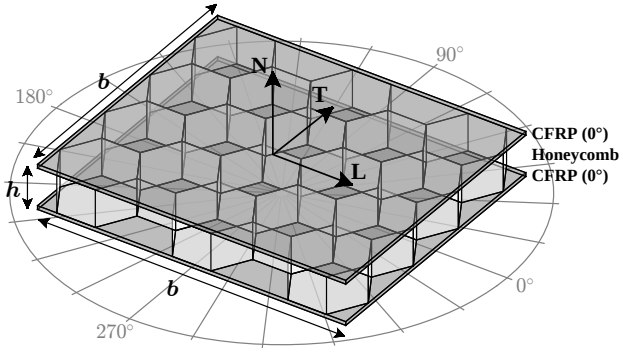

(a) Scheme of the plate. The two CFRP skins are oriented at 0°. h = 5.3 mm, b = 60 cm.

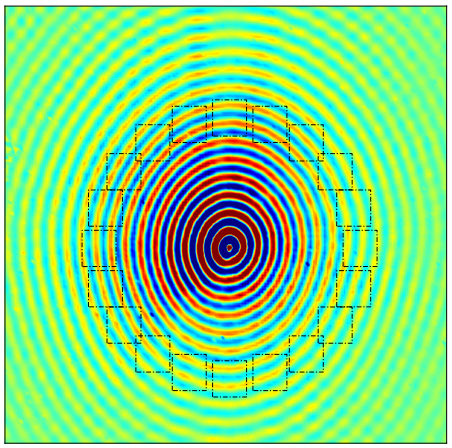

(b) Measured harmonic velocity field at the frequency of 25 kHz. 20 of the 100 zones used for the wavevector extraction are represented with dashed lines.

Figure 9: Sandwich plate with honeycomb core.

structure is symmetric with respect to the (xOz) and (yOz) planes, only the angles ranging from 0 to $\pi/2$ are represented.

These two figures allow a number of observations on the dynamical bending behavior of the structure. Focusing on $\boldsymbol{\kappa}$ identified at relatively low frequencies (from 5 kHz to 20 kHz), one can see a transition appearing between the two principal directions: at 5 kHz, waves propagating at 0° (Figure 10b in blue)

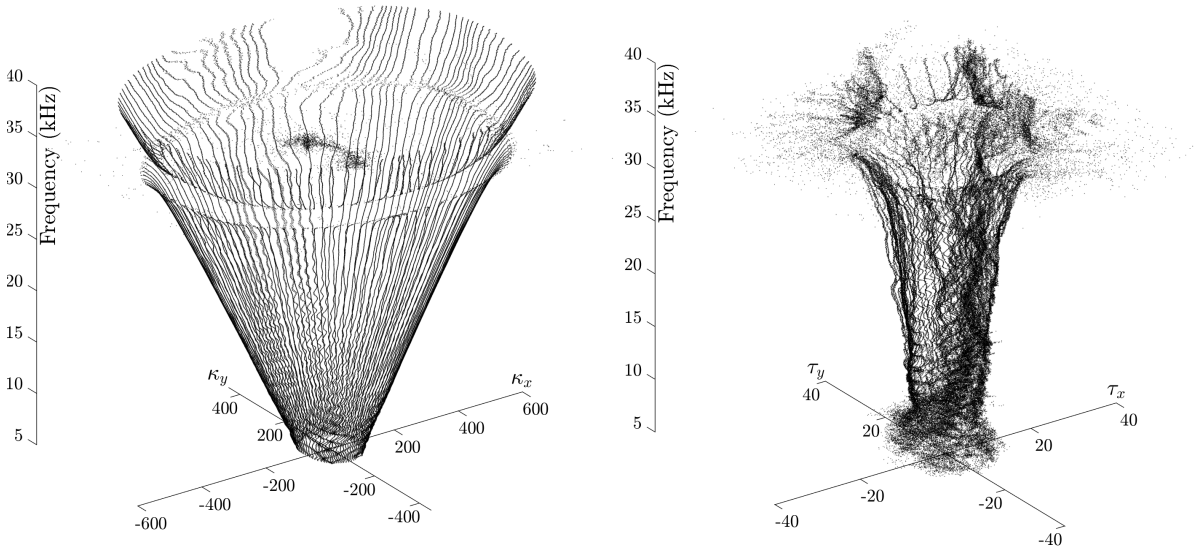

(a) Discrete dispersion surfaces. Left: real part $\boldsymbol{\kappa}$. Right: imaginary part $\boldsymbol{\tau}$.

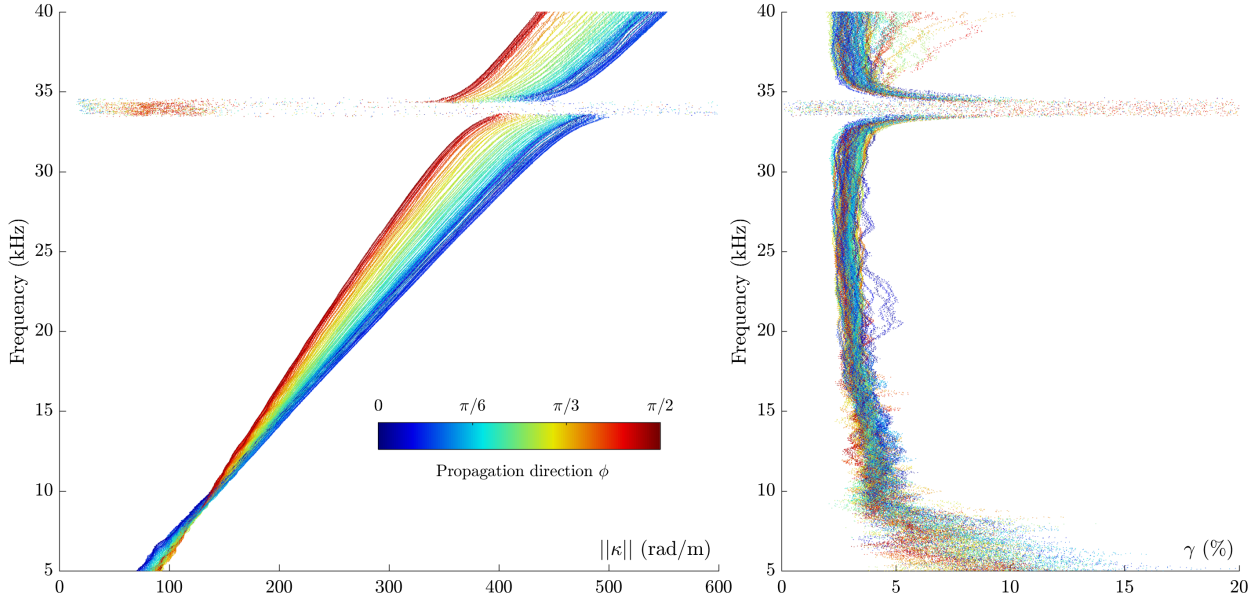

(b) Results of the HRWA as a function of frequency (y-axis) and propagation direction ϕ (marker color). Left: magnitude of the real part $\boldsymbol{\kappa}$ of the wavevectors; right: spatial decay γ (Eq. (5)).

Figure 10: Sandwich plate with honeycomb core. Results of the application of the HRWA.

are the fastest because the plate bending stiffness is governed by the carbon fiber skins. As the frequency increases, out-of-plane shear effects become significant and the wave velocity is more and more influenced by the honeycomb core properties. According to the results, the core seems to have its stiffest direction oriented at 90°: at 20 kHz, this direction corresponds to the lowest observed wavevector magnitude (in red). Regarding the extracted spatial decay γ, no significant influence of the wave propagation direction can be identified: from 10 kHz to 30 kHz, γ slowly decreases from 5% to 3%. As long as the measurement is sufficiently far from the source, it was observed that the distance as well as the size of the zone have a reduced influence on the estimation of this spatial decay.

The second important feature made visible by these representations is the presence of a singularity in the results around the frequency of 34 kHz in both the real and imaginary parts of the wavevectors. Just below this singularity, the half-wavelength $\pi/\|\boldsymbol{\kappa}\|$ ranges roughly from 6 mm to 8 mm, which corresponds approximately to the honeycomb cell size. Hence this singularity seems to be related to a resonance of the cells, drastically altering the propagation of waves and explaining the high spatial decay identified. Above this singularity, the spatial decay decreases down to approximately 3%.

Giving theoretical predictions of wave propagation in such a sophisticated periodic structure being outside the scope of the paper, no comparison is given here to confirm the observations or make quantitative identifications. However, it is clear from the results that the proposed HRWA seems to be a good candidate for the characterisation of structures with singular frequency-dependant behavior (i.e. for the identification of band-gaps in metamaterials).

3.3. Inhomogeneous composite plate

The preceding experience shows the possibility of the HRWA to perform a local wavevector extraction on small zones of the signal. For this third experimental study, this feature is used to identify the local specific bending stiffness. To this purpose, a 30cm wide laminated CFRP square plate with varying fiber directions was fabricated. The plate is made of 36 patches with various fiber directions. Figure 11a shows a top view of the plate, where the fiber directions θ are denoted by thin white lines. The stacking sequence is 4 ply, symmetric: $[\theta, 90°]_S$. The two central plies at 90°, continued on the entire plate, work as a substrate for the mechanical cohesion of the patches. Material properties of the carbon prepreg, identified from tensile tests, are summarized in Table 1.

For the measurements, the plate is excited from 500 Hz to 22 kHz with a shaker located in the bottom left corner. The velocity response is measured with a SLDV on a regular 100×100 mesh grid of points, sufficient to respect the Nyquist criterion.

The HRWA is applied to reduced zones of the measured signal, that correspond to each patch location. Indeed, the mechanical properties of the plate are homogeneous in each zone. The wavevector extraction is performed for each of the 1600 available harmonic response fields between 500 Hz and 22 kHz. Hence a collection of wavevectors is obtained for each patch, as a function of the frequency.

As the zones used for wavevector extraction are small and may be close to plate boundaries, evanescent waves can be detected. Theoretically such waves may be solutions of the dispersion laws, so could be used for the identification of the plate. However, in practice, the extraction of evanescent wavevectors is sensitive to noise. In order to enhance the identification performed afterwards, evanescent waves are removed with $\gamma_{\max} = 10$ % (Eq. (10)).

The largest wavevector magnitude extracted over all patches being around 580 rad/m, the minimum involved wavelength λ is approximately 11 mm, which gives a slenderness ratio $\lambda/h \approx 18$. As a consequence, the plate can be considered as a thin plate in the frequency range of interest. The dispersion equation of the bending waves of an anisotropic thin plate can be computed analytically following the Classical Lamination

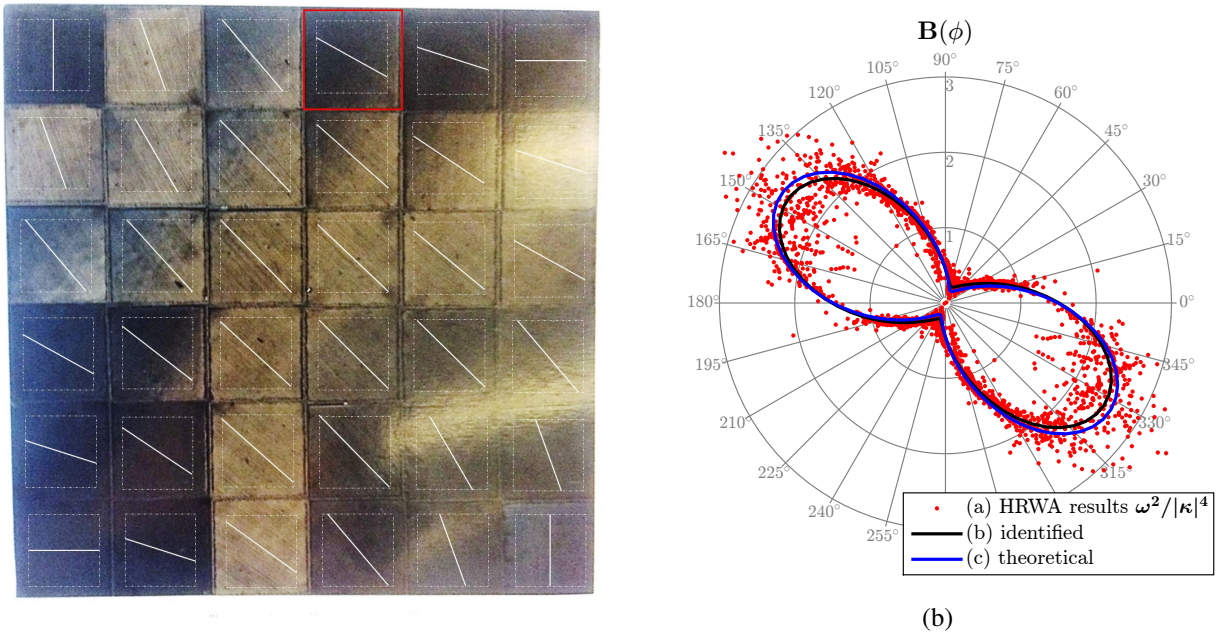

(a) (b)

Figure 11: Inhomogeneous CFRP plate. Identification of the local specific bending stiffness from HRWA results. (a) Top view of the plate (stacking sequence: $[\theta, 90°]_S$), which shows the fiber directions θ of the top carbon layer. The zone relative to the figure 11b is surrounded in red. (b) Local specific bending stiffness $B(\phi)$ (Eq. (12)): HRWA results (dot marks) ; least-Square fit of eq. 12 (black line) ; indicative theoretical diagram from material engineering constants of Table 1 (blue line).

Plate Theory (CLPT, see AppendixB). Assuming frequency-independent material properties, it can be recast to write the apparent specific bending stiffness B as a function of the wave propagation direction ϕ:

$$\begin{aligned} B(\phi) &= \frac{\omega^2}{|\boldsymbol{\kappa}(\omega,\phi)|^4} = \frac{D(\phi)}{M} \\ &= c^4 B_{11} + s^4 B_{22} + 2c^2 s^2 (B_{12} + 2B_{66}) \\ &\quad + 4c^3 s B_{16} + 4c s^3 B_{26} \end{aligned} \tag{12}$$

with

$$\begin{aligned} \boldsymbol{\kappa}(\omega,\phi) &= |\boldsymbol{\kappa}(\omega,\phi)| \cdot [c, s] \\ &= |\boldsymbol{\kappa}(\omega,\phi)| \cdot [\cos(\phi), \sin(\phi)] \end{aligned} \tag{13}$$

and

$$\begin{aligned} D_{ij} &= \frac{1}{3} \sum_c (h_{c+}^3 - h_{c-}^3)\, Q_{ij}^c \\ M &= \sum_c (h_{c+} - h_{c-}) \rho_c \end{aligned} \tag{14}$$

where c denotes the layer, Q_{ij}^c are the components of the plane stress stiffness matrix given by the carbon fiber mechanical properties and the fiber orientations, and (h_{c+}, h_{c-}) respectively denote the position of the top and bottom boundaries of the layer. From Eq. 12, an inverse problem can be formulated: given a collection of N real wavevectors $\boldsymbol{\kappa}_n = \kappa(\omega_n, \phi_n)\,[c_n\ s_n]^\top$, extracted with the HRWA in a local zone, the

vector of unknowns $\boldsymbol{b} = [B_{11}, B_{22}, B_{12} + 2B_{66}, B_{16}, B_{26}]^\top$ is solution of the system:

$$[\boldsymbol{a}_1 \ \dots \boldsymbol{a}_N]^\top \ \boldsymbol{b} = \left[\frac{\omega_1^2}{|\boldsymbol{\kappa}_1|^4} \ \dots \frac{\omega_N^2}{|\boldsymbol{\kappa}_N|^4} \right]^\top \tag{15}$$

$$\boldsymbol{a}_n = [c_n^4 \ \ s_n^4 \ \ 2c_n^2 s_n^2 \ \ 4c_n^3 s_n \ \ 4c_n s_n^3]^\top \tag{16}$$

As the number N of extracted wavevectors is usually of the order of thousands and only 5 unknowns b_i have to be determined, a Least-Square estimation can be performed. Since the right-hand side of Eq. (15) is strictly positive, B_{11}, B_{22} and $B_{12} + 2B_{66}$ are strictly positive too. By contrast, the coupling components B_{16} and B_{26} can be negative. An example of this local identification is shown in Figure 11b: for all frequencies, the wavevectors are extracted with the HRWA in the zone of the plate surrounded in red in Figure 11a. Experimental values of $\omega^2/|\boldsymbol{\kappa}|^4$ are denoted with dot marks in the polar diagram. The result of $\boldsymbol{B}(\phi)$ obtained with LS fitting (eq. 15) is plotted in black solid line. The identified specific bending stiffness is in good agreement with theoretical values (blue solid line), computed from material constants given in Table 1. The scattering in the values of B is mostly due to the amplification of the uncertainty by the fourth power of $|\boldsymbol{\kappa}|$ in Eq. 12. In addition, it can be observed that the dispersion of the experimental values is larger in the directions of high bending stiffness: indeed, in these directions, waves have long wavelengths (corresponding to small wavenumbers) compared to the width of the zone of interest: as consequence, the wavevector extraction is more sensitive to noise in these directions.

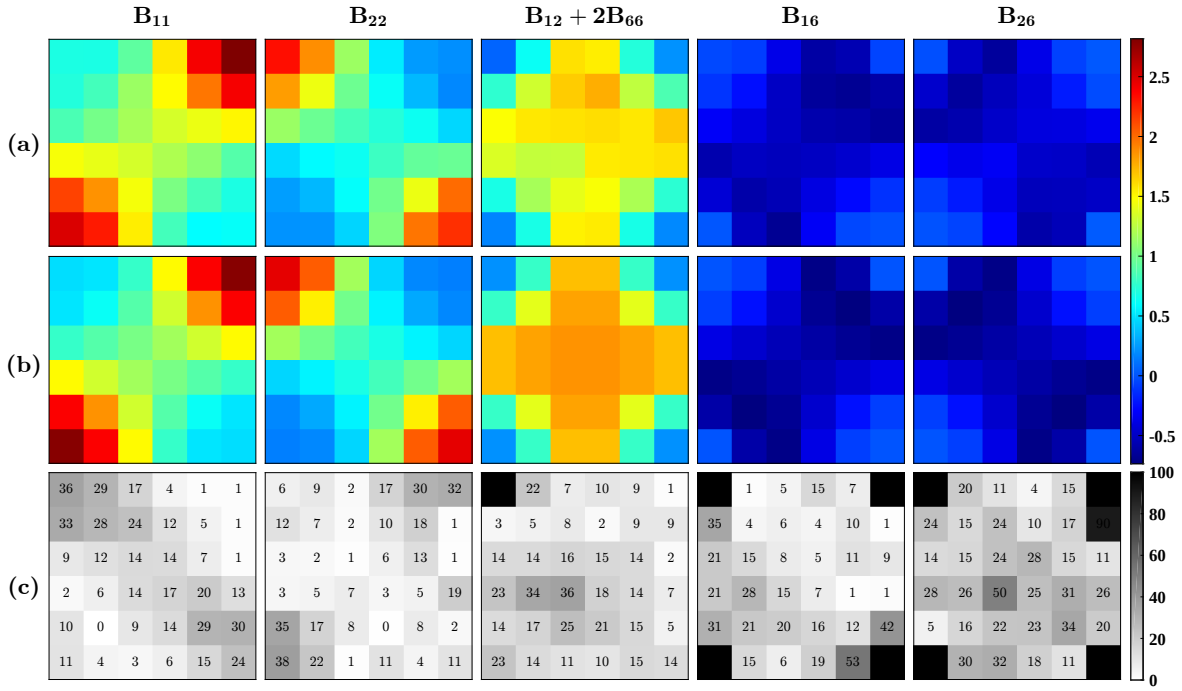

Figure 12: Inhomogeneous CFRP plate. Components of the local specific bending stiffness tensor $\boldsymbol{B}$, for each patch of the plate (see figure 11a). (a) Identified values from HRWA results (eq 15) ; (b) theoretical predictions from material properties in Table 1 ; (c) rounded relative errors (%), black is more than 100%.

The same procedure was repeated for each patch location of the plate, in order to identify the local specific bending stiffness tensor components. The results are shown in Figure 12: experimental values (a)

are compared with theoretical values (b), and relative errors are given (c). Globally it can be observed that the identification errors are smaller when the components are larger: for example, coupling components B_{16} and B_{26} are more sensitive to noise than diagonal constants (B_{11} and B_{22}). The relative error is particularly high (>200%) when theoretical components are equal to zero (black squares in Figure 12(c)). In addition, some differences can be explained by the uncertainties in the plate fabrication (patch angles and positions), and mechanical properties that differs from samples used for tensile tests in Table 1.

This last study shows the possibility to identify a local mechanical behavior on inhomogeneous anisotropic plates with a simple linear inverse problem.

4. Conclusions and Perspectives

The High-Resolution Wavevector Analysis (HRWA) was presented. It allows the characterization of the elastic behavior of composite plates. The implementation of the method, that makes use of the well-established signal processing ESPRIT algorithm and ESTER criterion, was summarized. By means of three experimental applications, the ability of the method to extract useful information from a measured kinematic field was illustrated. With the dependence of wavevectors as a function of the propagation direction and the frequency, the anisotropic behavior of the plate can be characterized for frequencies as low as the first modal frequencies. Various strain mechanisms such as bending, in plane shear or compression can be separated because of their distinct wavevectors and the ability of the algorithm to estimate the number of waves contained in the signal. In addition, the possibility to identify a local behavior in inhomogeneous plates with an inverse problem using extracted wavevectors in a small zone of the plate thanks to the high resolution of the procedure is shown.

Various applications can be considered. In particular, the extracted wavevectors can be used to formulate an inverse identification problem of the material properties, with refined plate models. The wide-frequency domain of validity of the method could be used to identify refined layer and inter-layer properties (individual lamina behavior, interface stiffness, delamination, etc.). The local wavevector extraction could be used as a characterization tool in emerging laying technologies, e.g. in *Automatic Fibre Placement (AFP)* process [57, 58]. In addition, it could be used to detect local defects in a fabricated plate, like damages or delaminations. Indeed, the extraction zones in the third example were chosen here to correspond to patch geometries; in a plate with continuously curved fibers, it could be possible to identify the local equivalent bending stiffness, by making the extraction zone slide continuously over the plate domain. At the end, a map of the mechanical properties of the plate could be represented, in order to find its defects.

As for now, a proper estimation of the wave decay can be achieved only in cases where the response field is close to a plane wave in its shape. This limits the ability to characterize the plate viscous behavior. This limitation is due to the signal model, which considers plane waves only (or *far-field* source). High-resolution algorithms suited for the identification of *near-field* sources has been developed [59, 60, 61], and could be used to identify the parameters of waves with a wavefront which is not plane. Moreover, uncertainties in the wavevector could be quantified by using results of the perturbation analysis of the ESPRIT algorithm [48].

Acknowledgments

This works is founded by the french National Research Agency (ANR), in the frame of the MAESSTRO project (*Modélisation Acoustique et Synthèse Sonore pour Tables d'haRmonie de pianOs*, ANR-14-CE07-0014). Since 2011, the Laboratoire Vibrations Acoustique is part of the LABEX CeLyA (ANR-10-LABX-0060) of Université de Lyon, within the program « Investissements d'Avenir » (ANR-11-IDEX-0007)

operated by the French National Research Agency (ANR). The authors would like to thank the reviewers, whose remarks contributed to the improvement of the present work.

AppendixA. Wavevector extraction procedure

AppendixA.1. The 2D-ESPRIT method

The 2D-ESPRIT methods deals with the estimation of the parameters $\boldsymbol{k}_r$ and a_r of the signal model $s(\boldsymbol{x})$ of equation 1. In this section, the signal order R is supposed to be known (see AppendixA.2). The corresponding signal matrix $\boldsymbol{S}$, of which components are the sampling of $s(\boldsymbol{x})$ along the grid $\boldsymbol{x}_{nm}$ (equation 6, 7 and Fig. 1), can be expressed as follows:

$$\boldsymbol{S} = \boldsymbol{U} + \boldsymbol{B} \tag{A.1}$$

with

$$\begin{aligned} S_{nm} &= u(\boldsymbol{x}_{nm}) + b(\boldsymbol{x}_{nm}) \\ &= \sum_{r=1}^{R} a_r \, z_{1,r}^{n} \, z_{2,r}^{m} + b(x_{nm}) \end{aligned} \tag{A.2}$$

where $\boldsymbol{U}$ and $\boldsymbol{B}$ matrices respectively denote the pure sum of decaying plane waves and the noise contribution in the signal and $z_{d,r} = \mathrm{e}^{\mathrm{i}k_{d,r}\Delta_d}$ the complex *signal poles*, with $d = 1, 2$.

AppendixA.1.1. Rotational Invariance Property

If the pure signal $\boldsymbol{U}$ is read by line $\boldsymbol{u} = \left[U_{11}\,,\ \ldots\,,\ U_{1L_2}\,,\ U_{21}\,,\ \ldots\,,\ U_{L_1L_2}\right]^\top$, it can be written in the form:

$$\boldsymbol{u} = \boldsymbol{V}\boldsymbol{a} \tag{A.3}$$

with $\boldsymbol{a} = \left[a_1, a_2, \ldots, a_R\right]^\top$. The Vandermonde matrix $\boldsymbol{V}$ used here is expressed as:

$$\boldsymbol{V} = \boldsymbol{V_1} \odot \boldsymbol{V_2} \tag{A.4}$$

where $\odot$ denotes the Khatri-Rao product [62] (column-wise Kronecker) and, for $d = 1, 2$:

$$\boldsymbol{V}_d = \begin{bmatrix} 1 & 1 & \cdots & 1 \\ z_{d,1} & z_{d,2} & \cdots & z_{d,R} \\ \vdots & \vdots & \ddots & \vdots \\ z_{d,1}^{L_d-1} & z_{d,2}^{L_d-1} & \cdots & z_{d,R}^{L_d-1} \end{bmatrix}_{L_d \times R} \tag{A.5}$$

The Vandermonde matrix satisfies a *rotational invariance* property. In the 2D-ESPRIT method, it is expressed as two recurrence relations between Vandermonde matrices built from two sub-parts of the signal. For each of the signal dimensions d :

$$\boldsymbol{V}^{\uparrow d} = \boldsymbol{V}^{\downarrow d}\,\boldsymbol{Z}_d \tag{A.6}$$

where $\boldsymbol{Z}_d = \mathrm{diag}(\{z_{d,1}, z_{d,2}, \ldots, z_{d,R}\})$. The superscripts $\downarrow d$ and $\uparrow d$ respectively denote the truncation of the first and the last index in the signal, in the direction d. As an example, the $\boldsymbol{V}^{\uparrow 1} = \boldsymbol{V}_1^{\uparrow} \odot \boldsymbol{V}_2$, where the $\boldsymbol{V}_1^{\uparrow}$ matrix is built from the $(L_1 - 1)$ first lines of $\boldsymbol{S}$.

As $\boldsymbol{S}$ is a noisy version of $\boldsymbol{U}$, this invariance property is not exactly satisfied by the measured signal. However, it can be estimated, which is the main purpose of the ESPRIT algorithm.

AppendixA.1.2. Autocovariance Matrix

From the n^{th} line of the signal $\boldsymbol{S}$, one can build the *Hankel* matrix $\boldsymbol{h}_n$ as follows:

$$\boldsymbol{h}_n = \begin{bmatrix} S_{n0} & S_{n1} & \cdots & S_{n(K_2-1)} \\ S_{n1} & S_{n2} & \cdots & S_{nK_2} \\ \vdots & \vdots & \ddots & \vdots \\ S_{n(N_2-1)} & S_{nN_2} & \cdots & S_{n(L_2-1)} \end{bmatrix}_{N_2 \times K_2} \tag{A.7}$$

where $N_2 = L_2 - K_2$.

From the signal $\boldsymbol{S}$, a *Hankel-block-Hankel* (HbH) matrix $\boldsymbol{H}$ is built, composed by the L_1 matrices $\boldsymbol{h}_n$:

$$\boldsymbol{H} = \begin{bmatrix} \boldsymbol{h}_0 & \boldsymbol{h}_1 & \cdots & \boldsymbol{h}_{K_1-1} \\ \boldsymbol{h}_1 & \boldsymbol{h}_2 & \cdots & \boldsymbol{h}_{K_1} \\ \vdots & \vdots & \ddots & \vdots \\ \boldsymbol{h}_{L_1-K_1-1} & \boldsymbol{h}_{L_1-K_1} & \cdots & \boldsymbol{h}_{L_1-1} \end{bmatrix}_{(N_1N_2)\times(K_1K_2)} \tag{A.8}$$

The role of the parameters K_d is discussed in the next section.

This HbH matrix is used to compute the autocovariance matrix of the signal:

$$\boldsymbol{C}_{SS} = \frac{1}{L_1 L_2} \boldsymbol{H}^* \boldsymbol{H} \tag{A.9}$$

AppendixA.1.3. Subspace decomposition

By computing the eigenvalue decomposition of the hermitian autocovariance matrix, signal and noise subspaces can be selected:

$$\boldsymbol{C}_{SS} = \boldsymbol{P}\,\boldsymbol{\Gamma}\,\boldsymbol{P}^{-1} \tag{A.10}$$

Without noise, the matrix $\boldsymbol{C}_{SS}$ would be rank R, but is full rank in the presence of noise. However, as it is an asymptotically unbiased estimator of the signal autocovariance, its eigenvectors are poorly sensitive to an uncorrelated noise b. As a consequence, by isolating the R first eigenvectors $\boldsymbol{p}_r$ of $\boldsymbol{C}_{SS}$, corresponding to its R dominant eigenvalues Γ_{rr}, the signal subspace $\boldsymbol{W} = [\boldsymbol{p}_1, \boldsymbol{p}_2, \ldots, \boldsymbol{p}_R]$ can be selected. The matrix $\boldsymbol{W}$ spans a signal subspace close to the subspace spanned by the Vandermonde matrix $\boldsymbol{V}$.

In the HbH matrix construction, (Eq. (A.7)) and (Eq. (A.8)), two parameters $\{K_d, d \in \{1, 2\}\}$ have to be chosen. Observing $\boldsymbol{C}_{SS}$ and $\boldsymbol{W}$ leads to the constraint $R \leq K_1K_2$. Kumaresan and Tufts [63] suggested to use these parameters to add $P = K_1K_2 - R$ virtual poles in the extraction, their role being to sample a potentially correlated noise contribution in $\boldsymbol{B}$, thus permitting to separate its influence in the extracted poles. In practice, the best strategy [64] consists in choosing a shape of $\boldsymbol{H}$ so that it is almost square, $K_d \approx L_d/2$.

AppendixA.1.4. Poles extraction

Since $\boldsymbol{V}$ and $\boldsymbol{W}$ matrix span close subspaces (not exactly the same because of noise), the transfer relation $\boldsymbol{V} = \boldsymbol{W}\,\boldsymbol{T}$ between them can be estimated. By integrating this relation in the rotational invariance (Eq. (A.6)), it comes:

$$\boldsymbol{Z}_d = \boldsymbol{T}^{-1}\,\boldsymbol{F}_d\,\boldsymbol{T} \tag{A.11}$$

with

$$\boldsymbol{F}_d = (\boldsymbol{W}^{\downarrow d})^{\dagger}\,\boldsymbol{W}^{\uparrow d} \tag{A.12}$$

where $\bullet^{\dagger}$ denotes the pseudo-inverse matrix. Therefore, the extraction of the poles $z_{d,r}$ could be achieved thanks to the diagonalization of the matrices $\boldsymbol{F}_d$. If the two diagonalizations were made independently, a

supplementary pairing step of the poles in the two directions would be necessary. Rouquette [38] suggested to jointly diagonalize the two matrices $\boldsymbol{F}_d$ related to the two signal dimensions, by the diagonalization of a single matrix $\boldsymbol{K}$:

$$\boldsymbol{K} = \beta\, \boldsymbol{F}_1 + (1-\beta)\, \boldsymbol{F}_2 = \boldsymbol{T}\, \boldsymbol{D}\, \boldsymbol{T}^{-1} \tag{A.13}$$

where the parameter β, arbitrary, is chosen different from $1/2$ (typically 0.55), in order to allow eigenvalues of multiplicity larger than 1. The wavevector extraction proved to be not sensitive to the parameter β.

Once $\boldsymbol{T}$ has been evaluated from $\boldsymbol{K}$, the equations A.11 are used to retrieve $\boldsymbol{Z}_d$, and finally the wavevectors:

$$\boldsymbol{k}_r = -\mathrm{i} \left[\frac{\ln(z_{1,r})}{\Delta_1}, \frac{\ln(z_{2,r})}{\Delta_2} \right] \tag{A.14}$$

If needed, the amplitudes a_r can be approximated by building the Vandermonde matrix $\boldsymbol{V}$ and solving the linear system of equations A.3 in the least-squares sense.

AppendixA.2. The 2D-ESTER criterion

The estimations of the two matrices $\boldsymbol{F}_d$ (equation A.12), made in the least-square sense, are sensitive to a wrong estimation of the signal order R. The ESTER criterion consists in searching the signal order R that minimizes the two errors of truncation $\Sigma_d(r)$, r being a candidate for the signal order:

$$\Sigma_d(r) = ||\boldsymbol{W}^{\downarrow d}(r)\, \boldsymbol{F}_d(r) - \boldsymbol{W}^{\uparrow d}(r)||_2 \tag{A.15}$$

In the present work, the geometrical mean of the two errors is used, so the two-dimensional ESTER criterion is expressed as:

$$R = \underset{r \in [\![\, 1, r_{\max}\,]\!]}{\arg\max} \left(\prod_d \Sigma_d(r) \right)^{-1/2} \tag{A.16}$$

In some applications of the ESTER criterion [46, 12, 44], a threshold parameter is added: the signal order is chosen as the largest value r for which the criterion reaches a local maximum larger than a fraction of the global maximum. In the present work, this strategy was not used.

AppendixA.3. Implementation of the wavevector extraction procedure

1. The Hankel-block-Hankel matrix $\boldsymbol{H}$ is built (Eq. (A.8)) from the signal $\boldsymbol{S}$ (Eq. (7)), with $K_d \approx L_d/2$
2. The autocovariance matrix $\boldsymbol{C}_{SS}$ is computed (Eq. (A.9)) and diagonalized
3. For each trial signal order $r \in [\![\, 1, r_{\max}\,]\!]$:
   (a) The signal subspace matrix $\boldsymbol{W}$ is built from the r dominant eigenvectors of $\boldsymbol{C}_{SS}$
   (b) The matrices $\boldsymbol{F}_d$, $d \in \{1, 2\}$ are computed (Eq. (A.12))
   (c) The two estimation errors $\Sigma_d(r)$ are evaluated (Eq. (A.15))

   The signal order R is finally estimated thanks to the ESTER criterion (Eq. (A.16)).
4. In order to evaluate the transfer matrix $\boldsymbol{T}$, the matrix $\boldsymbol{K}$ is assembled and diagonalized (Eq. (A.13))
5. The signal poles $\boldsymbol{Z}_d$ are extracted (Eq. (A.11))
6. Finally, the R complex wavevectors are deduced (Eq. (A.14)

AppendixB. Bending wave dispersion laws given by the Classical Lamination Plate theory.

The fourth-order differential equation of bending motion of a thin anisotropic plate, given by the Classical Lamination Plate Theory, with the out-of-plane displacement u_3 as unknown, is as follows:

$$D_{\alpha\beta\gamma\delta} u_{3,\alpha\beta\gamma\delta} + M\ddot{u}_3 = 0 \tag{B.1}$$

with Einstein notation for indices, $(\alpha, \beta, \gamma, \delta) \in \{1, 2\}$ and D and M defined by Equations 14. In order to get the dispersion law, the plane-wave approximation is taken. u_3 is then expressed as:

$$u_3(\boldsymbol{x}, t) = U_3 \, \mathrm{e}^{\mathrm{i}(\omega t - \boldsymbol{\kappa}\cdot\boldsymbol{x})}$$

Equation B.1 becomes:

$$\kappa_\alpha \kappa_\beta \kappa_\gamma \kappa_\delta D_{\alpha\beta\gamma\delta} - \omega^2 M = 0 \tag{B.2}$$

Using Voigt notation and Equation 13, the bending stiffness can be expressed as a function of the wave propagation ϕ:

$$\begin{aligned} D(\phi) &= M \frac{\omega^2}{|\boldsymbol{\kappa}(\omega, \phi)|^4} \\ &= c^4 D_{11} + s^4 D_{22} + 2c^2 s^2 (D_{12} + 2D_{66}) \\ &\quad + 4c^3 s D_{16} + 4c s^3 D_{26} \end{aligned} \tag{B.3}$$

References

[1] P. Margerit, A. Lebée, J.-f. Caron, X. Boutillon, High Resolution Wavenumber Analysis (HRWA) for the Mechanical Characterization of Viscoelastic Beams, Journal of Sound and Vibration.

[2] Z. Su, L. Ye, Y. Lu, Guided Lamb waves for identification of damage in composite structures: A review, Journal of Sound and Vibration 295 (3-5) (2006) 753–780.

[3] M. Kersemans, I. D. Baere, J. Degrieck, K. V. D. Abeele, L. Pyl, F. Zastavnik, H. Sol, W. V. Paepegem, Nondestructive damage assessment in fiber reinforced composites with the pulsed ultrasonic polar scan, Polymer Testing 34 (2014) 85–96.

[4] A. Katunin, K. Dragan, M. Dziendzikowski, Damage identification in aircraft composite structures : A case study using various non-destructive testing techniques, Composite Structures 127 (2015) 1–9.

[5] K. R. Hart, P. X. L. Chia, L. E. Sheridan, E. D. Wetzel, N. R. Sottos, S. R. White, Composites : Part A Mechanisms and characterization of impact damage in 2D and 3D woven fiber-reinforced composites, Composites Part A 101 (2017) 432–443.

[6] S. Phillips, L. Lessard, Application of natural fiber composites to musical instrument top plates, Journal of Composite Materials 46 (2) (2012) 145–154.

[7] A. Damodaran, L. Lessard, A. Suresh Babu, An Overview of Fibre-Reinforced Composites for Musical Instrument Soundboards, Acoustics Australia 43 (1) (2015) 117–122.

[8] S. Honda, Y. Narita, Vibration design of laminated fibrous composite plates with local anisotropy induced by short fibers and curvilinear fibers, Composite Structures 93 (2) (2011) 902–910.

[9] M. Montemurro, Y. Koutsawa, S. Belouettar, A. Vincenti, P. Vannucci, Design of damping properties of hybrid laminates through a global optimisation strategy, Composite Structures 94 (11) (2012) 3309–3320.

[10] A. Vincenti, P. Vannucci, M. R. Ahmadian, Optimization of laminated composites by using genetic algorithm and the polar description of plane anisotropy, Mechanics of Advanced Materials and Structures 20 (3) (2013) 242–255.

[11] D. O. Thompson, D. E. Chimenti, Review of progress in quantitative nondestructive evaluation, Vol. 18, Springer Science & Business Media, 2012.

[12] K. Ege, X. Boutillon, B. David, High-resolution modal analysis, Journal of Sound and Vibration 325 (4-5) (2009) 852–869.

[13] M. Rébillat, X. Boutillon, Measurement of relevant elastic and damping material properties in sandwich thick plates, Journal of Sound and Vibration 330 (25) (2011) 6098–6121.

[14] J.-M. Berthelot, Damping analysis of laminated beams and plates using the Ritz method, Composite Structures 74 (2) (2006) 186–201.

[15] M. Castaings, B. Hosten, T. Kundu, Inversion of ultrasonic, plane-wave transmission data in composite plates to infer viscoelastic material properties, NDT and E International 33 (6) (2000) 377–392.

[16] M. Kersemans, A. Martens, K. Van Den Abeele, J. Degrieck, L. Pyl, F. Zastavnik, H. Sol, W. Van Paepegem, The quasi-harmonic ultrasonic polar scan for material characterization: Experiment and numerical modeling, Ultrasonics 58 (2015) 111–122.
[17] J. G. Chen, N. Wadhwa, Y.-j. Cha, F. Durand, W. T. Freeman, Modal identification of simple structures with high-speed video using motion magnification, Journal of Sound and Vibration 345 (2015) 58–71.
[18] T. J. Beberniss, D. A. Ehrhardt, High-speed 3D digital image correlation vibration measurement : Recent advancements and noted limitations, Mechanical Systems and Signal Processing 86 (2017) 35–48.
[19] S. Rothberg, M. Allen, P. Castellini, D. Di Maio, J. Dirckx, D. Ewins, B. Halkon, P. Muyshondt, N. Paone, T. Ryan, H. Steger, E. Tomasini, S. Vanlanduit, J. Vignola, An international review of laser Doppler vibrometry: Making light work of vibration measurement, Optics and Lasers in Engineering (October) (2016) 0–1.
[20] J. Baqersad, P. Poozesh, C. Niezrecki, P. Avitabile, Photogrammetry and optical methods in structural dynamics – A review, Mechanical Systems and Signal Processing (2016) 1–18.
[21] F. Ablitzer, C. Pézerat, J.-M. Génevaux, J. Bégué, Identification of stiffness and damping properties of plates by using the local equation of motion, Journal of Sound and Vibration 333 (9) (2014) 2454–2468.
[22] Q. Leclère, F. Ablitzer, C. Pézerat, Practical implementation of the corrected force analysis technique to identify the structural parameter and load distributions, Journal of Sound and Vibration 351 (2015) 106–118.
[23] K. Ege, N. B. Roozen, Q. Leclère, R. G. Rinaldi, Assessment of the apparent bending stiffness and damping of multilayer plates; modelling and experiment, Journal of Sound and Vibration 426 (2018) 129–149.
[24] A. Berry, O. Robin, F. Pierron, Identification of dynamic loading on a bending plate using the Virtual Fields Method, Journal of Sound and Vibration 333 (26) (2014) 7151–7164.
[25] F. Pierron, M. Grediac, The Virtual Fields Method, Springer, 2011.
[26] J. Cuenca, F. Gautier, L. Simon, Measurement of the complex bending stiffness of a flat panel covered with a viscoelastic layer using the image source method, in: 8th European Conference on Noise Control 2009, EURONOISE 2009 - Proceedings of the Institute of Acoustics, Vol. 31, 2009.
[27] N. B. Roozen, Q. Leclère, K. Ege, Y. Gerges, Estimation of plate material properties by means of a complex wavenumber fit using Hankel's functions and the image source method, Journal of Sound and Vibration 390 (2017) 257–271.
[28] J. Berthaut, M. N. Ichchou, L. Jezequel, K-space identification of apparent structural behaviour, Journal of Sound and Vibration 280 (2005) 1125–1131.
[29] R. Cherif, J. D. Chazot, N. Atalla, Damping loss factor estimation of two-dimensional orthotropic structures from a displacement field measurement, Journal of Sound and Vibration 356 (2015) 61–71.
[30] P. J. Shorter, Wave propagation and damping in linear viscoelastic laminates, The Journal of the Acoustical Society of America 115 (5) (2004) 1917.
[31] R. Schmidt, A Signal Subspace Approach to Multiple Emitter Location and Spectral Estimation, Ph.D. thesis, Standford University (1981).
[32] Y. Hua, T. K. Sarkar, Matrix Pencil Method for Estimating Parameters of Exponentially Damped/Undamped Sinusoids in Noise, IEEE Transactions on Acoustics, Speech, and Signal Processing 38 (5) (1990) 814–824.
[33] R. Roy, A. Paulraj, T. Kailath, Estimation of signal parameters via rotational invariance techniques-ESPRIT, IEEE Transactions on Acoustics, Speech and Signal Processing 37 (7) (1989) 94–101.
[34] P. Van Overschee, B. L. De Moor, Subspace identification for linear systems: Theory—Implementation—Applications, Springer Science & Business Media, 2012.
[35] B. L. Ho, R. E. Kalman, Effective construction of linear state-variable models from input/output functions 1), at - Automatisierungstechnik 14 (1-12) (1966) 545–548.
[36] J.-n. Juang, R. S. Pappa, An Eigensystem Realization Algorithm for Modal Parameter Identification and Model Reduction, Journal of guidance, control, and dynamics 8 (5) (1985) 620–627.
[37] S. Shahbazpanahi, S. Valaee, M. H. Bastani, Distributed source localization using ESPRIT algorithm, IEEE Transactions on Signal Processing 49 (10) (2001) 2169–2178.
[38] S. Rouquette, M. Najim, Estimation of frequencies and damping factors by two-dimensional ESPRIT type methods, IEEE Transactions on Signal Processing 49 (1) (2001) 237–245.
[39] V. Emiya, B. David, R. Badeau, A parametric method for pitch estimation of piano tones, ICASSP, IEEE International Conference on Acoustics, Speech and Signal Processing - Proceedings 1.
[40] R. Badeau, B. David, R. Boyer, Eds Parametric Modeling And Tracking Of Audio Signals, Proceedings of 5th Int. conf. on Digital Audio Effects (DAFx02 (2002) 26–28.
[41] A. Chaigne, C. Lambourg, Time-Domain Simulation of Damped Impacted Plates - I - Theory and Experiments, Journal of the Acoustical Society of America 109 (4) (2001) 1422–1432.
[42] J.-l. L. Carrou, F. Gautier, R. Badeau, J.-l. L. Carrou, F. Gautier, R. Badeau, Sympathetic string modes in the concert harp To cite this version : HAL Id : hal-00945199, Acta Acustica united with Acustica 95 (4) (2009) 744–752.

[43] K. Ege, X. Boutillon, M. Rébillat, Vibroacoustics of the piano soundboard: (Non)linearity and modal properties in the low- and mid-frequency ranges, Journal of Sound and Vibration 332 (5) (2013) 1288–1305.
[44] V. Fréour, F. Gautier, B. David, M. Curtit, Extraction and analysis of body-induced partials of guitar tones, The Journal of the Acoustical Society of America 138 (6) (2015) 3930–3940.
[45] R. Badeau, B. David, G. Richard, High-resolution spectral analysis of mixtures of complex exponentials modulated by polynomials, IEEE Transactions on Signal Processing 54 (4) (2006) 1341–1350.
[46] R. Badeau, B. David, G. Richard, A new perturbation analysis for signal enumeration in rotational invariance techniques, IEEE Transactions on Signal Processing 54 (2) (2006) 450–458.
[47] K. Liu, J. P. C. da Costa, H. Cheung So, L. Huang, Subspace techniques for multidimensional model order selection in colored noise, Signal Processing 93 (2013) 1976–1987.
[48] S. Sahnoun, K. Usevich, P. Comon, Multidimensional ESPRIT: Algorithm, Computations and Perturbation Analysis, Tech. rep. (2016).
[49] B. A. Auld, Acoustic fields and waves in solids, Krieger Publishing Company, 1973.
[50] J. Laroche, The use of the matrix pencil method for the spectrum analysis of musical signals, The Journal of the Acoustical Society of America 94 (4) (1993) 1958–1965.
[51] S. Rouquette, Y. Berthoumieu, M. Najim, An efficient subband decomposition based on the Hilbert transform for high-resolution spectral estimation, in: Proceedings of Third International Symposium on Time-Frequency and Time-Scale Analysis (TFTS-96), IEEE, pp. 409–412.
[52] S. Sahnoun, K. Usevich, P. Comon, Multidimensional ESPRIT for Damped and Undamped Signals: Algorithm, Computations, and Perturbation Analysis, IEEE Transactions on Signal Processing 65 (22) (2017) 5897–5910.
[53] E. Barbieri, A. Cammarano, S. De Rosa, F. Franco, Waveguides of a Composite Plate by using the Spectral Finite Element Approach, Journal of Vibration and Control 15 (3) (2009) 347–367.
[54] I. Bartoli, A. Marzani, F. Lanza di Scalea, E. Viola, Modeling wave propagation in damped waveguides of arbitrary cross-section, Journal of Sound and Vibration 295 (3-5) (2006) 685–707.
[55] A. Lebée, K. Sab, Homogenization of cellular sandwich panels, Comptes Rendus Mécanique 340 (4-5) (2012) 320–337.
[56] M. C. Junger, D. Feit, Sound, structures, and their interaction, Vol. 225, MIT press Cambridge, MA, 1986.
[57] H.-J. L. Dirk, C. Ward, K. D. Potter, The engineering aspects of automated prepreg layup: History, present and future, Composites Part B: Engineering 43 (3) (2012) 997–1009.
[58] P. Ribeiro, H. Akhavan, a. Teter, J. Warmi ski, A review on the mechanical behaviour of curvilinear fibre composite laminated panels, Journal of Composite Materials 48 (22) (2013) 2761–2777.
[59] Y. Zhong, S. Yuan, L. Qiu, Multiple damage detection on aircraft composite structures using near-field MUSIC algorithm, Sensors and Actuators, A: Physical 214 (2014) 234–244.
[60] S. Yuan, Y. Zhong, L. Qiu, Z. Wang, Two-dimensional near-field multiple signal classification algorithm-based impact localization, Journal of Intelligent Material Systems and Structures 26 (4) (2015) 400–413.
[61] T. Qiu, P. Wang, A Novel Method for Near-Field Source Localization in Impulsive Noise Environments, Circuits, Systems, and Signal Processing 35 (11) (2016) 4030–4059.
[62] C. G. Khatri, C. R. Rao, Solutions to some functional equations and their applications to characterization of probability distributions, Sankhy{\=a}: The Indian Journal of Statistics, Series A (1968) 167–180.
[63] R. Kumaresan, D. Tufts, Estimating the parameters of exponentially damped sinusoids and pole-zero modeling in noise, Acoustics, Speech and Signal Processing, IEEE Transactions on 30 (6) (1982) 833–840.
[64] S. Sahnoun, K. Usevich, P. Comon, S. Sahnoun, K. Usevich, P. Comon, Optimal choice of Hankel-block-Hankel matrix shape in 2-D parameter estimation, [Research Report] GIPSA-lab.